

# We are IntechOpen, the world's leading publisher of Open Access books Built by scientists, for scientists

6,900

Open access books available

186,000

International authors and editors

200M

Downloads

Our authors are among the

154

Countries delivered to

TOP 1%

most cited scientists

12.2%

Contributors from top 500 universities



WEB OF SCIENCE™

Selection of our books indexed in the Book Citation Index  
in Web of Science™ Core Collection (BKCI)

Interested in publishing with us?  
Contact [book.department@intechopen.com](mailto:book.department@intechopen.com)

Numbers displayed above are based on latest data collected.  
For more information visit [www.intechopen.com](http://www.intechopen.com)



# Laser Shock Peening: Modeling, Simulations, and Applications

Y.B. Guo

*Dept. of Mechanical Engineering,  
The University of Alabama,  
Tuscaloosa, AL 35487  
U.S.A.*

## 1. Introduction

Laser shock peening (LSP) is a surface treatment process to improve surface integrity and fabricate micro surface structures. The mechanism of LSP is shown in Figure 1. LSP is a cold mechanical process where pressure waves caused by expanding plasma plastically deform the surface of a material. LSP uses a thin layer of ablative material that is opaque to the laser. The opaque ablative material, typically black spray paint or tape, is used as a sacrificial layer in the early study by Fairland and Clauer (Fairland & Clauer, 1976). The sacrificial layer also minimizes undesirable thermal effects on the surface caused by the laser. The laser partially vaporizes the ablative layer to form high pressure plasma. The plasma, confined by a thin layer of water film, expands rapidly resulting in a recoiling pressure wave on the order of GPa reported by Fairland et al. (Fairland et al., 1972), Fabbro et al. (Fabbro et al., 1990), Masse and Barreau (Masse & Barreau, 1995), Berthe et al. (Berthe et al., 1997), Fan et al. (Fan et al., 2005), Warren, et al. (Warren et al., 2008), and Caslaru, et al. (Caslaru et al., 2008). The pressure wave is the cold mechanical process that plastically deforms the surface. The plasma-induced shock pressure on the order of GPa can be much larger than the dynamic yield strength of the work material. Once the peak pressure exceeds material yield strength, the transient shock pressure causes severe plastic deformation, refined grain size, compressive residual stresses, and increased hardness at the surface and in the subsurface. As a result, the mechanical properties on the workpiece surface are enhanced to improve the performance of fatigue, wear, corrosion and foreign object damage.

Besides producing favorable surface integrity, LSP can also be used to fabricate various micro surface structures such as dent arrays using an automatic x-y positioning system. The micro surface structures may have various functions. For example a laser peened dent array can act as lubricant reservoirs to reduce coefficient of friction in bearings and to reduce flow drag of compressor blades.

Just due to the transient nature of shocking pressure, real time in-situ measurement of laser/material interaction is very challenging. A numerical simulation method may provide an ideal tool to shed light on the process mechanics and resultant surface integrity.

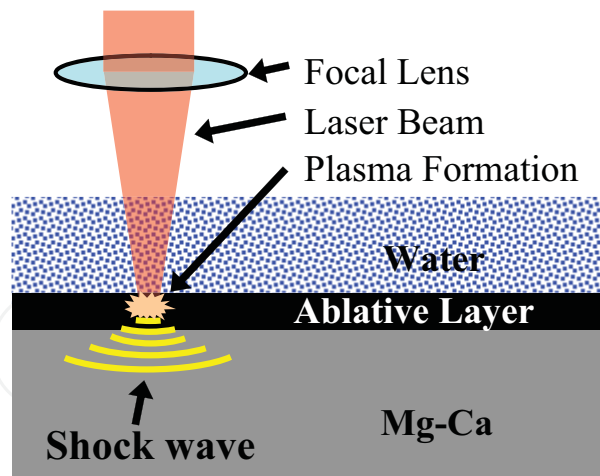


Fig. 1. Process principle of micro dent fabrication by LSP

## 2. State-of-the-art of LSP simulation

### 2.1 LSP for enhanced surface integrity

LSP is a surface treatment process to modify surface properties for improved wear and fatigue performance. LSP is primarily conducted on metallic components. The principle of LSP is to use a high intensity laser and suitable overlays to generate high pressure shock waves on the workpiece surface.

An increase in fatigue strength is achieved by large magnitudes of compressive residual stresses which develop in the subsurface. The maximum compressive residual stress is usually on the surface and decreases with depth. The transient shock waves can also induce microstructure changes near the surface and cause high density of dislocations. The combined effect of the microstructure changes and dislocation entanglement contribute to improved surface properties.

It has been shown by previous research (Clauer et al., 1983; Clauer & Koucky, 1991; Peyre et al., 1996; Vaccari, 1992; Ashley, 1998; Brown, 1998; Banas et al., 1990) that improved fatigue life of metallic components such as bearings, gears, shafts, etc can be accomplished by inducing compressive residual stress using LSP. An advantage of LSP is that the affected depth is very deep ( $\approx 1$  mm) as compared with other surface treatment processes such as conventional shot peening.

During LSP (Figure 1), the sample surface is first coated with a thin layer of material such as black paint which is opaque to the laser beam. This opaque layer acts as sacrificial material and is converted to high pressure plasma as it absorbs energy from a high intensity laser (1-10 GW/cm<sup>2</sup>) for very short time durations (< 100 ns). If the sample surface is also submerged in a transparent media such as water, the rapidly expanding plasma cannot escape and the resulting shock wave is transmitted into the sample subsurface. The shock pressure can be much larger than the dynamic yield strength of the material (>1 GPa), which causes surface plastic deformation and compressive residual stresses which can extend to a deep depth ( $\approx 1$  mm) in the subsurface. Due to the high strains/strain rates that the material experiences, there can also be significant microstructure changes thus causing the surface properties such as hardness, strength, and fatigue strength to be improved. Because thermal rise in the sample is nearly eliminated by the water overlay, LSP is primarily a cold working process.

A significant amount of LSP research has been conducted to investigate the surface integrity. Most experimental work has focused on the determination of residual stress magnitudes and distributions in the near surface. The effect of LSP on surface properties and fatigue life has been relatively less studied. The resulting surface integrity can be correlated with the LSP process parameters such as laser intensity, laser spot size, peening pass, and peening spacing. The following is a brief overview of previous research results.

Residual stress can vary with LSP process parameters. Increasing the laser intensity increases both the magnitude and affected depth of compressive stress in the subsurface. However, it has been shown that laser intensities greater than a particular threshold serve to decrease the surface stress magnitude, but continue to increase the magnitude and affected depth in the subsurface (Peyre et al., 1996). This was attributed to expansion release waves that are formed due to high energy shock waves. An investigation of laser spot size effect showed that energy attenuation is less for larger spot sizes allowing the stress shock wave to propagate deeper into the material (Fabbro et al., 1998). Thus larger spot sizes increase the depth of plastic deformation. A study of overlapped laser spots (Clauer & Koucky, 1991; Peyre et al., 1996; Peyre et al., 1998; Ruschau et al., 1999) showed that the residual stress distribution is nearly uniform and is entirely compressive.

Previous numerical simulations of LSP have been performed to gain better understanding of the physical process. Because LSP is a highly transient process, it is difficult (if not impossible) to experimentally observe and quantify the stress wave propagation into the sample surface. Simulations have been used to aid in determining accurate shock pressure models, verify experimental data, and predict residual stress profiles. Zhang et al. (Zhang et al., 2004) improved the shock pressure models by Clauer (Clauer & Holbrock, 1981) and Fabbro (Fabbro et al., 1990) by accounting for the non-linear mass transfer of LSP. The model also accounts for the time dependent radial expansion of plasma for micro sized laser peening. Finite element simulations have been performed to verify and predict residual stress profiles after LSP (Braisted & Brockman, 1999; Ding, 2003; Zhang & Yao, 2002).

## **2.2 LSP fabrication of micro dent arrays**

The controlled patterning of solid surfaces improves the wear, friction and lubrication (Anderson et al., 2007). Micro dents serve as fluid reservoirs that effectively retain lubricant. Also micro dents function as traps for wear debris, eliminating a potential plowing effect caused by entrapped particles. The long term benefit of surface patterning is to extend the life of contacting surfaces. Micro dents on the surface can improve the surface lifetime by a factor of ten (Romano et al., 2003). Experimental studies on the effect of dent patterns on micro-grooved sapphire discs lead to the conclusion that fabricated micro dents on metallic surfaces is a useful method to reduce friction in sliding contact. Manufacturing techniques to fabricate micro dents arrays on component surfaces include micro indentation (Nakatsuji & Mori, 2001), micro-drilling (Friedrich, 2002), and laser ablation (Etsion, 2005). These processes often induce surface damage such as cracks and phase transformation which may shorten component life. A new process to make dents while avoid material damage is highly needed. When the pressure exceeds the dynamic yield stress in LSP, plastic deformation occurs and forms a dent on the surface. LSP is a flexible and economic technique to fabricate micro dent arrays on metallic component surfaces using an automatic x-y positioning system.

### 2.3 LSP biomaterials

Biodegradable implants are a relatively new and emerging form of treatment for common bone ailments. Biodegradable implants are useful to the healing process due to the ability to gradually dissolve and absorb into the human body after implantation. The development of biodegradable implants has had a beneficial effect on in-vivo treatment of patients with various bone ailments.

Currently, biodegradable implants are mainly made of polymers, such as poly-L-Lactic acid. However, these polymer based implants usually have an unsatisfactory mechanical strength. An alternative to biodegradable polymer implants is permanent metallic implants composed of steel or titanium alloys. Permanent metal implants have superior strength compared to polymers. As a consequence, metal implants are often too stiff resulting in a stress shielding effect that can be damaging to the healing process (Benli et al., 2008; Completo et al., 2008; Au et al., 2007; Shi et al., 2007; Isaksson & Lerner, 2003; Nagels et al., 2003; Gefen, 2002). Stress shielding occurs when bone is shielded by an implant from carrying load. As a result, the bone tends to weaken over time resulting in more damage. To minimize the effects of stress shielding on the human body while still retaining strength, a soft lightweight metal is required. Therefore, Mg alloys are proposed as an ideal biodegradable implant material due to its biocompatibility and superior strength to weight ratio compared to that of other biomaterials.

Magnesium is an element essential to the human body. Intake of a certain amount of magnesium (300 ~ 400 mg/day) is normally required for regular metabolic activities (Seiler, 1987). The direct corrosion product of magnesium,  $Mg^{2+}$ , is easily absorbed or consumed by the human body (Song, 2007). However, the rapidly generated by-products of magnesium corrosion, such as hydrogen gas and hydroxides, are not physiologically favorable. Hydrogen evolution and alkalinization resulting from corrosion of Mg are the most critical obstacles in using magnesium as an implant material. A straightforward strategy to tackle these difficulties is to control the corrosion rate of a biodegradable magnesium implant. The adjustment of surface property is one promising solution to control the corrosion rate of Mg in human body.

In this chapter, calcium (Ca) was alloyed with Mg to form a Mg-Ca alloy. It is well known that Ca is a major component in human bone and is also essential in chemical signaling with cells (Ilich & Kerstetter, 2000). Ca has a low density ( $1.55 \text{ g/cm}^3$ ) such that when alloyed with Mg, the density is similar to that of bone. The Ca in Mg-Ca alloys produces hydroxyapatite (HA) as a corrosion product on the surface of the implant. HA mineral is a naturally occurring form of calcium apatite with the formula  $Ca_{10}(PO_4)_6(OH)_2$  and has close resemblance to the chemical and mineral components of teeth and bone. As a result of this similarity it stimulates bone cells to attack the implant surface and make proper bonding (Aksakal & Hanyaloglu, 2008), which allows for fractured segments to realign in correct anatomical position which is critical to recovery.

Laser shock peening (LSP) is a promising surface treatment technique to improve the surface integrity by imparting compressive residual stresses that are beneficial for controlling corrosion of Mg-Ca implants. LSP has been initiated to fabricate an array of dents on component surfaces (Warren et al., 2005; Warren & Guo, 2007; Caslaru et al., 2008; Sealy & Guo, 2008). Previous finite element analyses (FEA) of LSP investigate individual peening of a metal substrate. FEA of single peens neglects the effect of neighboring dents on topography, hardness and residual stress. The purpose of this chapter is to determine the

effects of sequential peening of Mg-Ca alloy on surface topography as well as predict the residual stress profile. Sequential peening experiments and simulations were performed and compared to single peening experiments and simulations.

### 3. LSP modeling and simulation procedures

#### 3.1 Modeling of 3D spatial and temporal shock pressure

Because the laser spot is circular, a two-dimensional finite element simulation can not reflect the true nature of LSP. For this reason a 3D model must be used for realistic simulation of the laser induced shock pressure. The simulation mesh is shown in Figure 2. The mesh has two regions with different mesh densities. With a high mesh density, the results from a simulation converge to a unique solution. As expected, the area where the pressure is applied contains a higher mesh density than the outer regions of the model. The dense mesh region consists of elements of  $1\ \mu\text{m}$  cubes. Micron elements provide a suitable spatial resolution of the output variables.

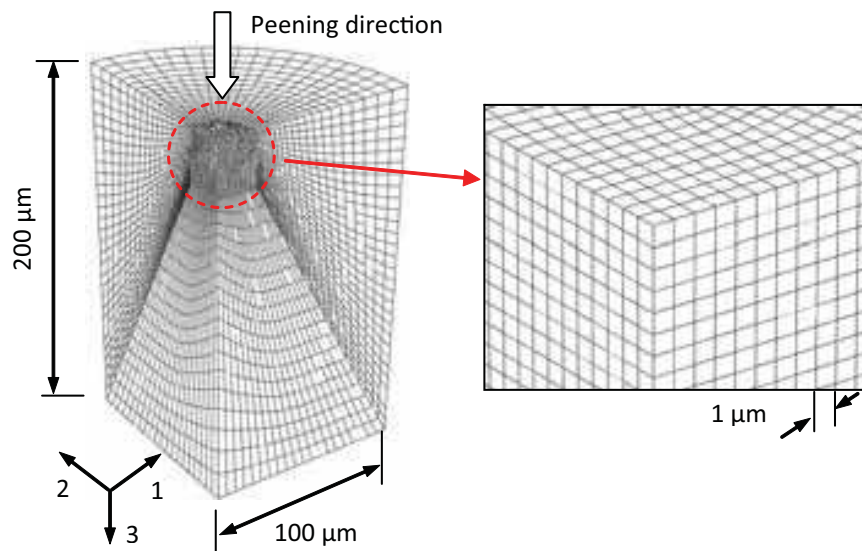


Fig. 2. Three-dimensional (3D) FEA simulation of LSP

The spatial and temporal pressure distribution during LSP is neither uniform nor linear. For this reason a subroutine VDLOAD was used to apply the non-uniform shock pressure. The subroutine allows the pressure intensity to vary simultaneously with respect to radial distance from the center of the laser spot and elapsed time of the laser pulse. It works by assigning local origins at the center of the desired shock peen locations and calculates the radial distance to each node surrounding this new origin from the equation of a circle as

$$r = \sqrt{(\text{curcoord}(i,1))^2 + (\text{curcoord}(i,2))^2} \quad (1)$$

where  $\text{curcoord}(i,1)$  and  $\text{curcoord}(i,2)$  are the coordinates in the 1 and 2 directions, respectively, for the current node at each time increment of the analysis.

The pressure as a function of radial distance from the center of the laser spot follows a Gaussian distribution (Zhang et al., 2004). Maximum pressure is located at the center of the laser spot and decreases with increasing radial distance from the center.

The pressure distribution is also a function of the elapsed time of laser pulse. The pressure is initially zero and reaches a peak value when the elapsed time equals the total pulse time. Following the results by Zhang, et al. (Zhang et al., 2004), the pressure versus time can be well represented as fourth order polynomials to follow the pressure vs. time relationships shown in Figure 3.

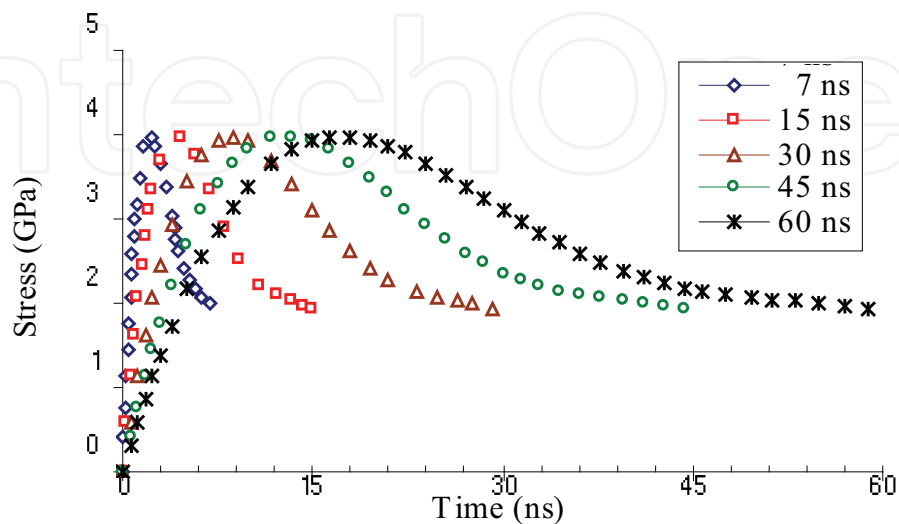


Fig. 3. Theoretical pressure vs. time curve

The pressure  $P(r,t)$  at any point and time can be calculated as

$$P(r,t) = P(t) \exp\left(-\frac{r^2}{2R^2}\right) \quad (2)$$

where  $P(t)$  is the pressure at time  $t$  during the laser pulse interpolated from Figure 3,  $r$  is the radial distance from the center of the laser spot in Eq. (1), and  $R$  is the laser spot radius.

### 3.2 Modeling of dynamic mechanical behavior

Due to the extremely high strain rates ( $> 10^6 \text{ s}^{-1}$ ) that occur during LSP, traditional material models are not adequate. For this reason a subroutine VUMAT was used to incorporate the plasticity/failure model developed by the internal state variable (ISV) plasticity model (Bammann et al., 1993; Bammann et al., 1996). The BCJ constitutive equations can be written below.

$$\dot{\underline{\sigma}} = \dot{\underline{\sigma}} - \underline{W}^e \underline{\sigma} + \underline{\sigma} \underline{W}^e = \lambda \text{tr}(\underline{D}^e) \underline{I} + 2\mu \underline{D}^e \quad (3)$$

$$\underline{D}^e = \underline{D} - \underline{D}^p \quad (4)$$

$$\underline{D}^p = f(T) \sinh\left[\frac{\|\underline{\sigma} - \underline{\alpha}\| - \{R + Y(T)\}}{V(T)}\right] \frac{\underline{\sigma} - \underline{\alpha}}{\|\underline{\sigma} - \underline{\alpha}\|} \quad (5)$$

$$\begin{aligned}\dot{\underline{\alpha}} &= \dot{\underline{\alpha}} - \underline{\mathbf{W}}^e \underline{\alpha} + \underline{\alpha} \underline{\mathbf{W}}^e \\ &= h(T) \underline{\mathbf{D}}^p - \left[ \sqrt{\frac{2}{3}} r_d(T) \|\underline{\mathbf{D}}^p\| + r_s(T) \right] \|\underline{\alpha}\| \underline{\alpha}\end{aligned}\quad (6)$$

$$\dot{R} = H(T) \underline{\mathbf{D}}^p - \left[ \sqrt{\frac{2}{3}} R_d(T) \|\underline{\mathbf{D}}^p\| + R_s(T) \right] R^2 \quad (7)$$

The evolution equations (6) and (7) for the internal state variables  $\underline{\alpha}$  and  $R$  are motivated from dislocation mechanics and are in a hardening-minus-recovery format. The kinematic hardening internal state variable  $\underline{\alpha}$  representing directional hardening is related to the dislocations in cell interior. The variable captures the softening effect due to unloading, also termed as Bauschinger's effect. The isotropic hardening internal state variable  $R$  is related to the dislocations in walls and it captures the continued hardening at large strains. The use of internal state variables and the evolution equations enable the prediction of strain rate history and temperature history effects.

The model uses nine temperature dependent functions to describe the inelastic response. They can be classified into three basic types: those associated with the initial yield, the hardening functions, and the recovery functions. The rate-independent yield stress  $Y(T)$ , the rate-dependence of initial yield stress  $f(T)$ , and the magnitude of rate-dependence of yield stress  $V(T)$  are assumed to be of the forms

$$V(T) = C_1 \exp(-C_2 / T) \quad (8)$$

$$Y(T) = C_3 \exp(C_4 / T) ([1 + (\tanh(C_{19}(C_{20} - T)))] / 2) \quad (9)$$

$$f(T) = C_5 \exp(-C_6 / T) \quad (10)$$

The three functions of  $r_d(T)$ ,  $h(T)$ ,  $r_s(T)$  describe the tensor or kinematic hardening and recovery, which can be thought of as the center of yield surface. The functions of  $R_d(T)$ ,  $H(T)$ , and  $R_s(T)$  describe the scalar or isotropic hardening and recovery, which can be thought of as the radius of the yield surface.

$$r_d(T) = C_7 \exp(-C_8 / T) \quad (11)$$

$$h(T) = C_9 - C_{10}T \quad (12)$$

$$r_s(T) = C_{11} \exp(-C_{12} / T) \quad (13)$$

$$R_d(T) = C_{13} \exp(-C_{14} / T) \quad (14)$$

$$H(T) = C_{15} - C_{16}T \quad (15)$$

$$R_s(T) = C_{17} \exp(-C_{18} / T) \quad (16)$$

The material constants ( $C_1 - C_{20}$ ) can be determined by fitting the BCJ model to the baseline test data using a non-linear square fitting method. The very short pulse duration ( $< 100$  ns) makes the simulation an ideal transient case. For this purpose, Abaqus/Explicit (HKS, 2008) was used to implement the simulation scheme.

#### 4. Simulation case studies

3D finite element simulation models in peening several engineering materials have been developed to investigate transient laser/material interactions at nano timescale during peening. Three application case studies in automotive, aerospace, and biomedical industries are presented using the developed simulation method.

##### 4.1 Case 1: LSP simulation of enhancing surface integrity of hardened steel

The purpose of this case study is to micro laser shock peening hardened AISI 52100 steel (62 HRc) by varying the laser pulse duration (time elapsed for maximum pressure) for times of 5, 10, 50, and 100 ns. For comparative purposes, a conventional material model which uses experimental compression stress/strain data and the failure/plasticity model termed the ISV model is used to predict the material behavior. The results will provide insight into the highly transient LSP process and assist in proper selection of experimental parameters for control of surface integrity requirements after LSP.

The fitted material constants are shown in Table 1. The simulation was performed as a single pass of laser shock peening with a laser spot radius of  $6 \mu\text{m}$ . The simulated laser intensity is  $5.5 \text{ GW/cm}^2$  which attains a maximum pressure of  $\approx 4 \text{ GPa}$ . The laser pulse time was varied as 5, 10, 50, and 100 ns in order to test the effect of strain rate on the transient stress and strain.

BCJ Parameter	Material Constants	BCJ Parameter	Material Constants
C1 (MPa)	1.00E+00	C11 (s/MPa)	2.39E-03
C2 (K)	1.00E+00	C12 (K)	4.00E+02
C3 (MPa)	2.52E+03	C13 (1/MPa)	5.00E-02
C4 (K)	5.85E+01	C14 (K)	0.00E+00
C5 (1/s)	1.00E+00	C15 (MPa)	1.50E+02
C6 (K)	-1.20E+04	C16 (MPa/K)	-1.40E+01
C7 (1/MPa)	4.00E-02	C17 (s/MPa)	2.70E-03
C8 (K)	0.00E+00	C18 (K)	0.00E+00
C9 (MPa)	5.60E+03	C19	4.15E-03
C10 (MPa/K)	9.00E+00	C20 (K)	6.65E+02

Table 1. ISV material constants of AISI 52100 steel

The greatest magnitude (stress or strain) during the simulation was retrieved across and beneath the laser spot as shown in Figure 4. This allows direct comparison of various laser pulse times on the transient behavior of the material during LSP. For comparative purposes, the results are plotted for simulations using the BCJ model and direct data input in table format (hereafter "Table") which use only compression stress/strain data for modeling material behavior.

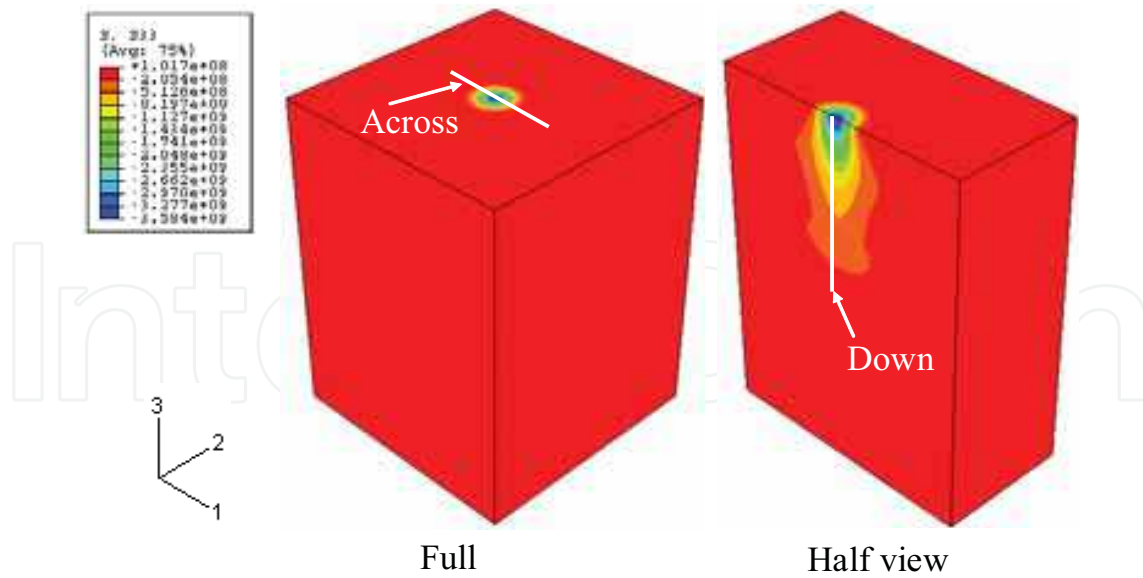


Fig. 4. Result path locations

**4.1.1 Stress distributions**

The maximum subsurface normal stress in the peening direction is shown in Figure 5a. The maximum stress occurs on the surface for the greater pulse times (50 ns and 100 ns) while it occurs in the subsurface ( $\approx 3.5 \mu\text{m}$ ) for the lower pulse times (5 ns and 10 ns). This may be due to higher strain rates generated by the shorter pulse times. However, the stress at all depths greater than  $3.5 \mu\text{m}$  is more compressive for the shorter pulse durations. It is observed that the subsurface stress difference at the same depth can be as much as 750 MPa between the shortest and longest laser pulse times. Another observation is the consistently higher stress (at depths  $> 3.5 \mu\text{m}$ ) predicted by the BCJ model than that for simulations using table format. This is reasonable due to the extremely high strain rates during LSP for which there is no experimental data available. At pulse times of 50 ns and 100 ns, the strain rate has less influence and the stress distribution curves are nearly identical for the BCJ model and table format.

The maximum normal stress across the specimen surface is shown in Figure 5b. From the figure it is observed that the difference between the experienced surface stress at the laser center can be as large as 1.0 GPa by varying the laser pulse time. However, the difference is negligible beyond the diameter of the laser spot ( $12 \mu\text{m}$ ).

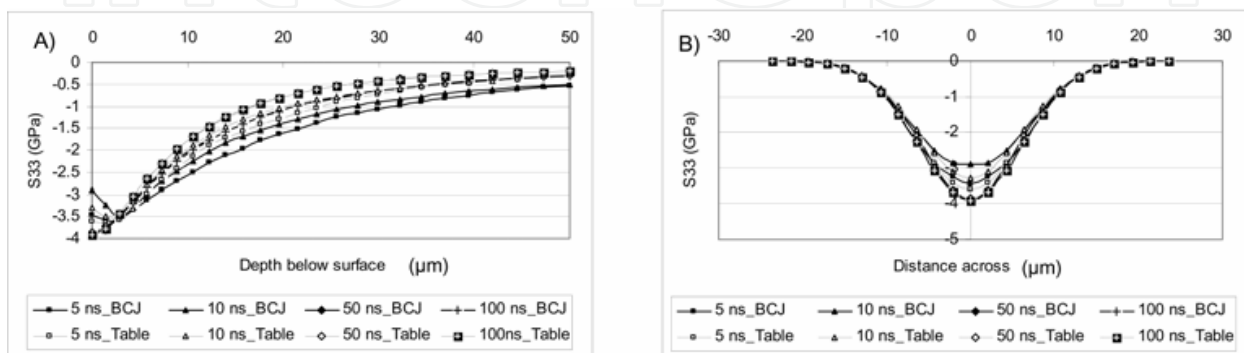


Fig. 5. Stress variation (peening direction a) down and b) across

The subsurface von Mises profile is shown in Figure 6a. The maximum value of von Mises stress occurs at a depth of  $4.2 \mu\text{m}$  for all simulation cases. It is also observed that the stress magnitude is inversely proportional to the laser pulse time. The difference between the 5 ns and 10 ns pulse times is, however, much larger (500 MPa) than for the 50 ns and 100 ns cases (50 MPa) at the surface showing that the relationship is not linear. In addition, the variation of the stress for the 5 ns and 10 ns pulse is larger than that for the 50 ns and 100 ns pulse times when comparing the BCJ model and table format.

Figure 6b shows the von Mises distribution across the top surface. The trend is similar to that of the transverse normal stress that the largest magnitude occurs across the entire surface by order of decreasing pulse time. A sharp rise in von Mises stress occurs across a diameter of  $\approx 24 \mu\text{m}$  reaching a maximum at the center of the laser spot. The influence of the high strain rate induced by the 5 ns pulse is seen by the 30% higher equivalent stress when compared to the next pulse time (10ns).

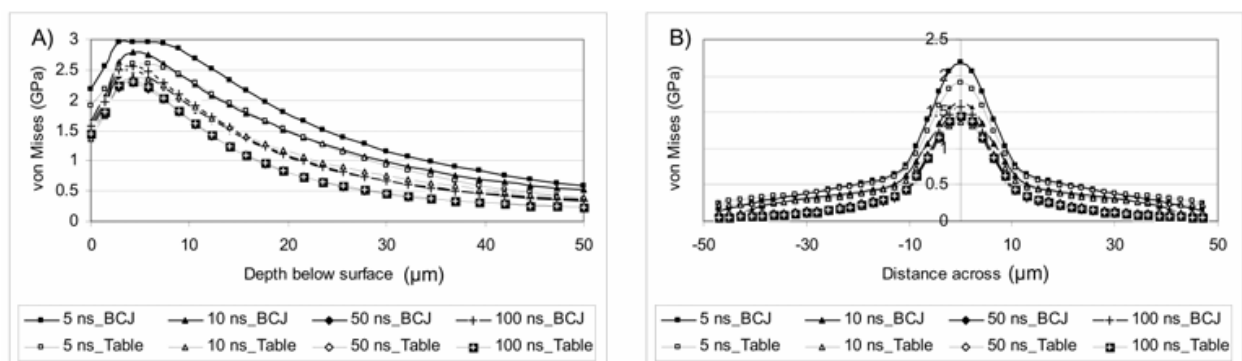


Fig. 6. Von mises variation a) down and b) across

#### 4.1.2 Strain rate

The maximum strain occurred in the loading direction and is shown in Figure 7a. For each case, the greatest strain magnitude occurred in the subsurface, the depth of which is dependent on the pulse duration. For the 10, 50, and 100 ns cases, the maximum value occurred at a depth of  $\approx 2.8 \mu\text{m}$ , while the 5 ns case reached a maximum strain of  $-1.87 \times 10^{-2}$  at a depth of  $4.3 \mu\text{m}$ . After the maximum strain is reached, the strain magnitude decreases with the highest value occurring at each depth in order of decreasing pulse duration.

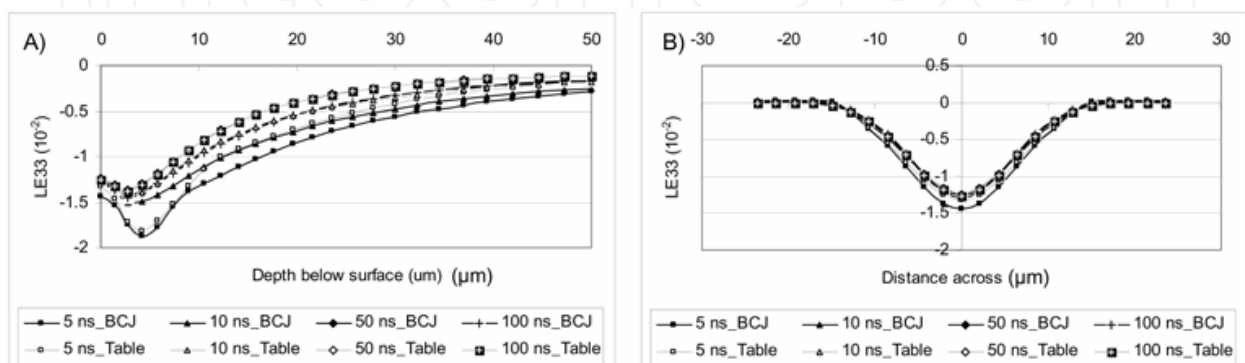


Fig. 7. Strain variation a) down and b) across

The maximum strain in the loading direction across the surface is shown in Figure 7b. The maximum value of  $-1.4 \times 10^{-2}$  was attained for the 5 ns pulse time using the BCJ model. A  $\approx 7\%$  lower strain was predicted by the table format for each simulation pulse time. The maximum strain attained by the 10, 50, and 100 ns cases was  $\approx -1.2 \times 10^{-2}$ .

#### 4.1.3 Residual stress

The predicted residual stresses were obtained from the surface element located at the center of the laser spot. A comparison of the measured and simulated residual stress values are shown in Figure 8. Both the predicted and measured residual stresses are compressive, so they agree with the nature and trend. There is some discrepancy between the two which may be due to several factors that differentiate the experimental procedure from the simulation. In addition to numerical errors, the first is the massive parallel LSP used for the experiment which was not accounted for in the benchmark simulation. The overlaps of consecutive laser peenings that occurred in LSP experiments would increase the magnitudes of compressive residual stress. The predicted residual stresses from both single and two LSP passes are expected to be lower than those from the experiments. The second is that the x-ray diffraction technique using  $\text{Cr}_{K\alpha}$  radiation actually measures an average residual stress in the depth of x-ray penetration (5-10  $\mu\text{m}$ ). In addition, the exact location of residual stress measurement with regard to the laser peened zone can not be accurately controlled for the experiment. For the measurement itself, the residual stress magnitudes across the peened surface are different just due to the nonuniform nature of surface integrity. Unless high precision calibration and control can be carried out first, the x-ray and other non-destructive measurement methods are only useful for comparative purpose.

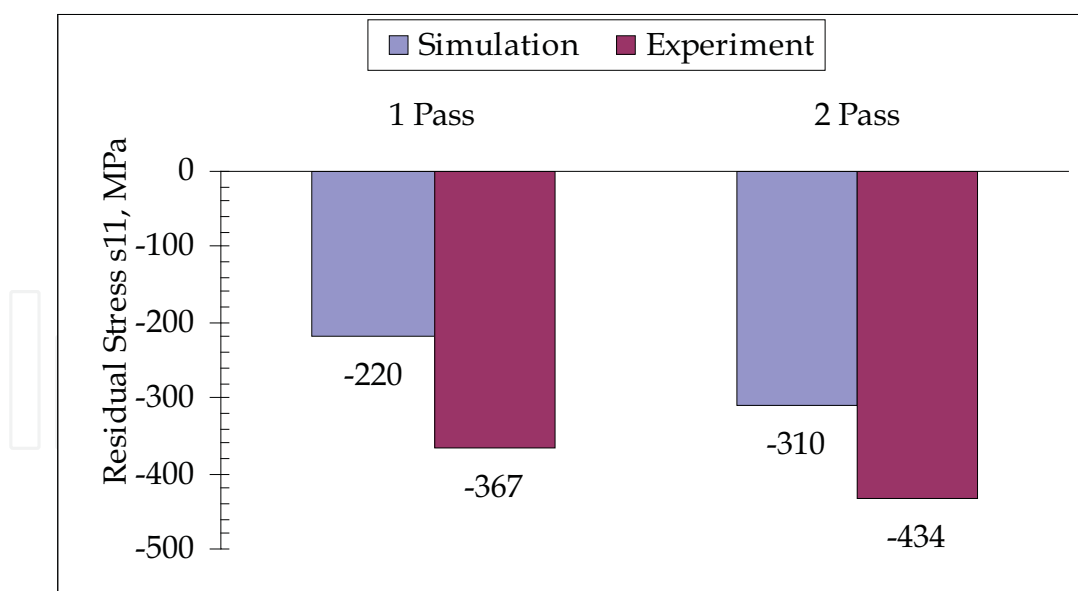


Fig. 8. Comparison of predicted surface residual stress  $s_{11}$  with measured data

#### 4.2 Case 2: LSP simulation of fabricating micro dent arrays on titanium surface

A 3D finite element simulation model was developed to fabricate micro dent arrays on titanium Ti-6Al-4V surfaces as shown in Figure 2, for improving tribology performance. Ti-6Al-4V is a widely used engineering material in aerospace, automotive, and biomedical

industries. Micro surface structures of the LSP processed Ti-6Al-4V components is critical for product performance. However, the surface deformation and mechanical behavior in patterning a Ti-6Al-4V surface has not been well understood. The simulation aims to understand the laser/material interaction and the related mechanical phenomena. The material constants ( $C_1 - C_{20}$ ) were determined by fitting the ISV model to the baseline test data using a non-linear square fitting method. The fitted material constants are shown in Table 2 (Guo et al., 2005). The modulus of elasticity for Ti-6Al-4V is 114 GPa. Poisson's ratio is 0.34 at room temperature. The density is 4430 kg/m<sup>3</sup>.

ISV parameter	Material constants	ISV parameter	Material constants
C1 (MPa)	1.0	C11 (s/MPa)	205
C2 (K)	0.2	C12 (K)	0
C3 (MPa)	1570	C13 (1/MPa)	1.9E-3
C4 (K)	10	C14 (K)	0
C5 (1/s)	1.0E-5	C15 (MPa)	619
C6 (K)	0	C16 (MPa/K)	3.8E-1
C7 (1/MPa)	7.0E-2	C17 (s/MPa)	5.0E-4
C8 (K)	0	C18 (K)	0
C9 (MPa)	1866	C19	1.0992E-3
C10 (MPa/K)	0.3	C20 (K)	876

Table 2. ISV material constants of Ti-6Al-4V

#### 4.2.1 Simulated dent geometry

Figure 9a depicts the dent profiles for the various pulse times. Each dent was measured 50 ns after the simulation. Initially, increasing the pulse time leads to an increase in depth. However, the 30 ns simulation has the maximum depth at 0.9  $\mu\text{m}$ . The simulations with pulse times greater than 30 ns exhibited a decrease in the depth. This suggests there is an optimal pulse time which produces the deepest dents given a peak pressure.

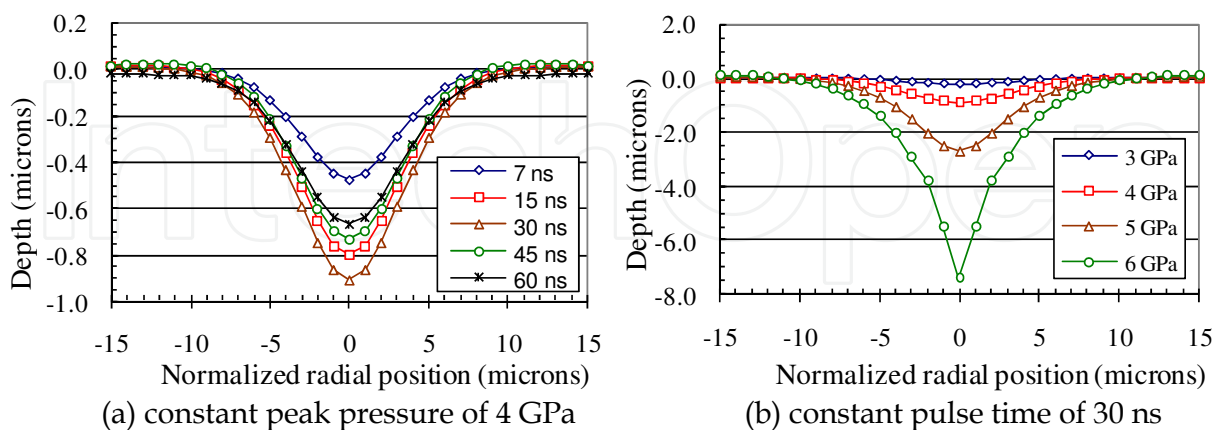


Fig. 9. Simulated dent profiles

Figure 9b shows the dent profiles as the peak pressure increases. There is a non-linear relationship between the dent depth and peak pressure. As the load increases, the depth of the dent increases as well. However, the radius of each dent is about 20 microns. A comparison between the simulated dent contours and measured ones will be conducted in a future study.

#### 4.2.2 Surface material behavior at different peening time

Material behaviors at the surface are characterized by the stress/strain graphs along the peening or depth direction (axis-3). Each stress/strain profile plotted represents the maximum transient stress/strain during the peening process. The corresponding radial curves are corresponding stress/strain graphs where the maximum occurs along the depth.

**Transient stress profiles:** Von Mises stress along the depth is plotted in Figure 10a. In each simulation, the maximum von Mises is 1.45 GPa and occurs about 3  $\mu\text{m}$  below the surface and gradually decreases to 1.27 GPa. The stress then sharply decreases toward zero as the depth increases. Surface material at different peening times experiences similar von Mises characteristics but at different depths. Figure 10b shows von Mises profile in the radial direction 3  $\mu\text{m}$  in the subsurface. In the radius of 9  $\mu\text{m}$ , the von Mises stress remains greater than 1.2 GPa. Then, the stress begins to decrease exponentially.

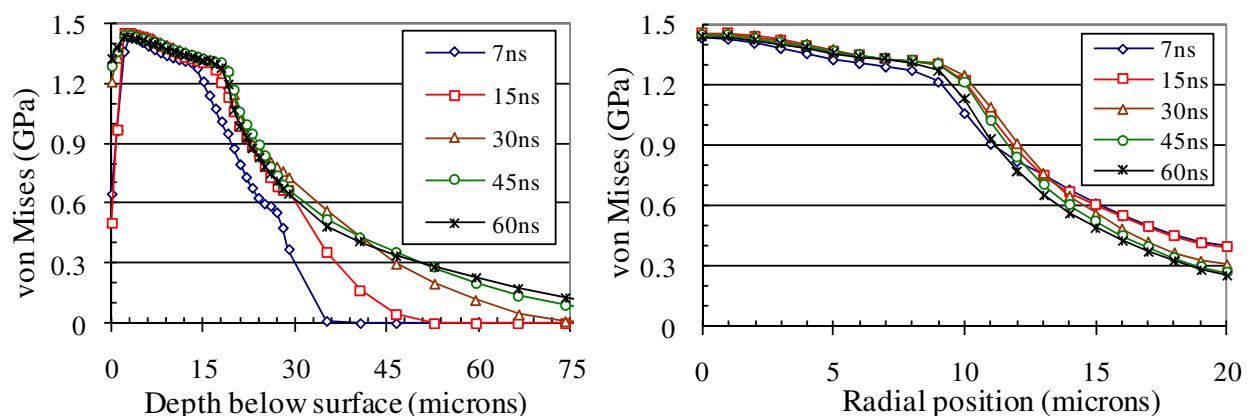


Fig. 10. von Mises stress distributions at different peening time

**Transient strain profiles:** The effective plastic strain PEEQ along the depth, Figure 11a, exhibits an inverse relationship with the peening time. The plastic strain decreases with the increased peening time. However, below the surface that is not the case. The 30 ns peening time induces the maximum plastic strain. PEEQ converges to zero at 15  $\mu\text{m}$  to 20  $\mu\text{m}$  in subsurface. Figure 11b illustrates the radial profiles of PEEQ which extends 10  $\mu\text{m}$  in the radial direction.

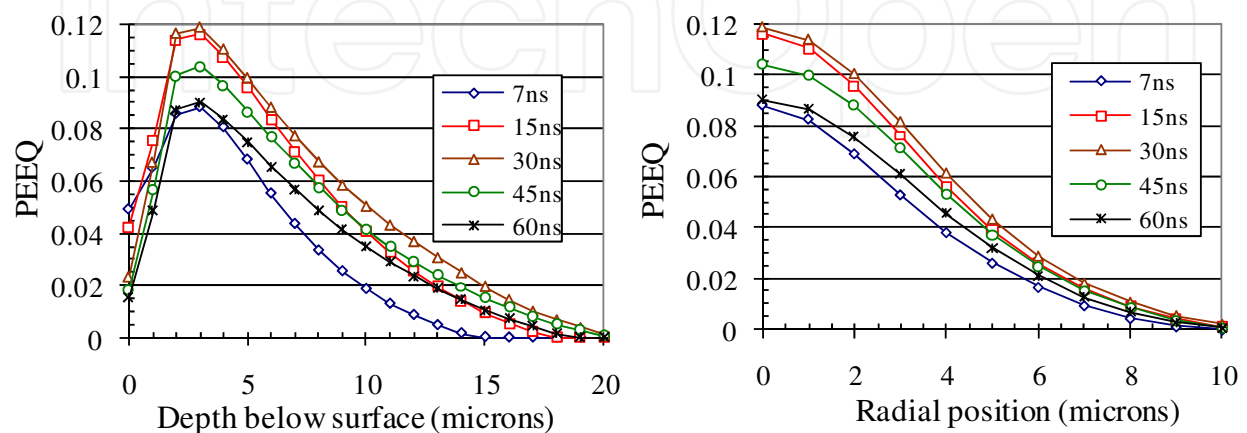


Fig. 11. Effective plastic strain distributions at different peening time

**Strain rate profiles:** Figure 12a shows the strain rate along the depth for each peening time. Material at the 7 ns peening case experiences the largest strain rate at  $31 \times 10^6/s$  at  $3 \mu m$  in the subsurface. As peening time increases, the strain rate decreases non-linearly. In each case, the peak rate occurs at 2 to  $3 \mu m$  below the surface. Figure 12b shows the radial profiles of the strain rate which extends approximately  $10 \mu m$  from the peening center. The strain rate for the 7 ns case converges more rapidly in the radial direction than other cases.

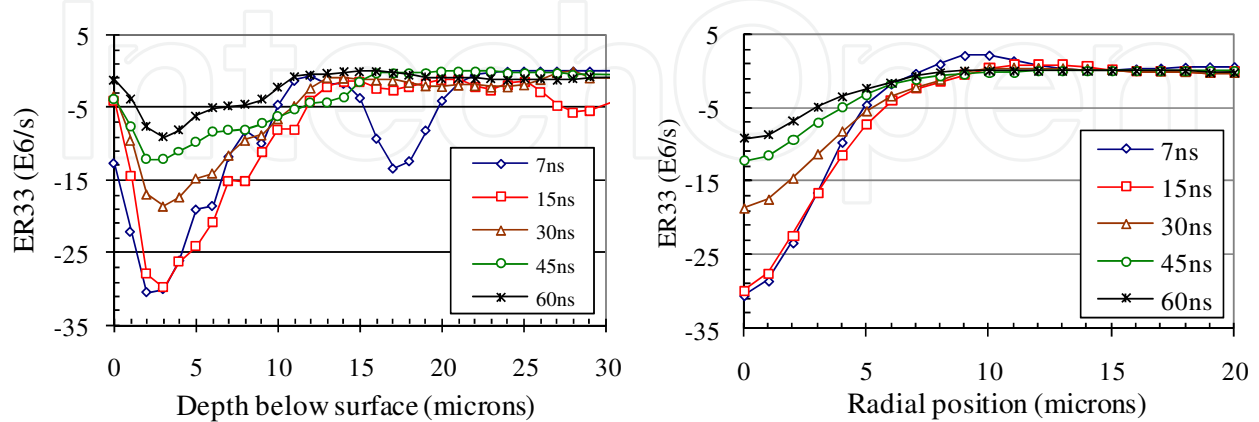


Fig. 12. Strain rate distributions at different peening time

#### 4.2.3 Surface material behavior at different peening pressure

**Transient stress profiles:** Von Mises profiles in the depth are plotted in Figure 13a. At peak pressures 3 GPa and 4 GPa, the maximum von Mises occurs at  $3 \mu m$  in the subsurface. As peak load increases the maximum von Mises moves toward the surface. It is also observed that von Mises profiles overlap at peak pressures 5 GPa and 6 GPa. It implies that increasing the peak pressure over 6 GPa will saturate von Mises stress. Initially, the stress gradually decreases along the depth. Once it decreases to 1.3 GPa, it rapidly drops and converges toward zero. Figure 13b shows the stress along the radial direction. It exhibits a similar phenomenon seen in the depth direction.

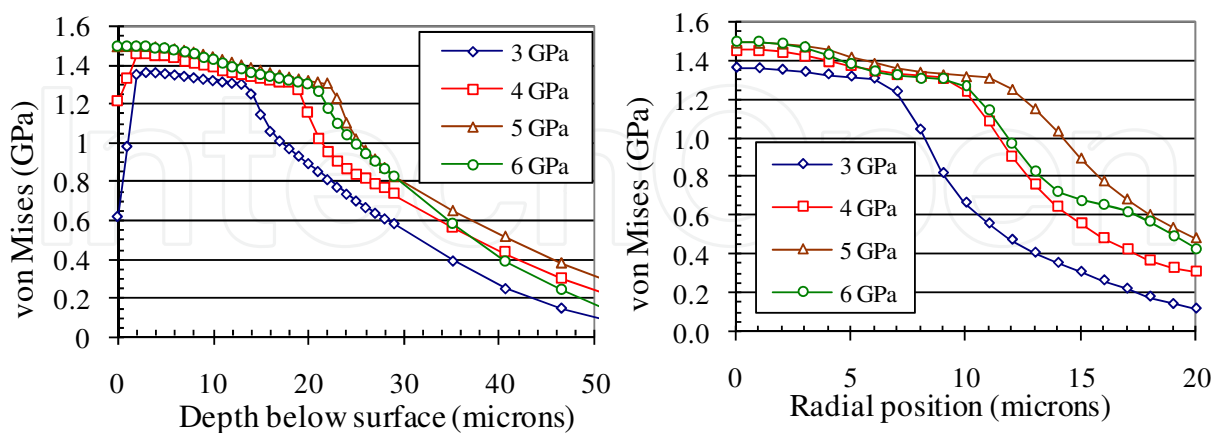


Fig. 13. von Mises stress distributions at different peening pressure

**Strain profiles:** The equivalent plastic strain in the depth is plotted in Figure 14a. The maximum plastic strain at 6 GPa peak pressure is on the surface, while it moves deeper into the subsurface as the peak load decreases. For example, it moves to  $3 \mu m$  deeper for the case of 3 GPa peak pressure. The corresponding radial profiles for PEEQ are shown in Figure 14b.

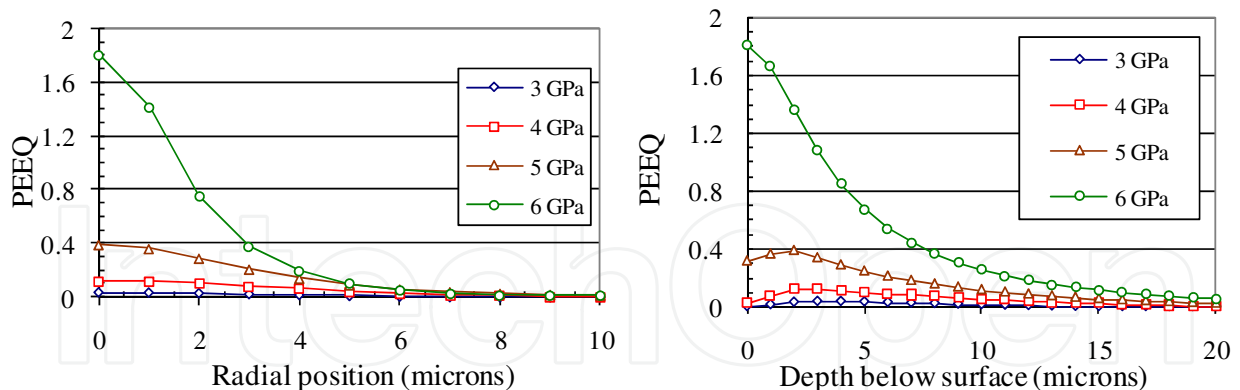


Fig. 14. Effective plastic strain distributions at different peening pressure

**Strain rate profiles:** Figure 15a shows that the maximum strain rate is  $226 \times 10^6/s$  on the surface at 6 GPa peak pressure. As peak pressure decreases, the maximum strain rate moves deeper below the surface. In addition, the simulations at peak pressures of 3 GPa and 4 GPa experienced much smaller strain rates ( $< 2 \times 10^6$ ) on the surface. But the maximum strain rates occur at 3  $\mu m$  in the subsurface. The corresponding radial profiles of the strain rate in Figure 15b extend approximately 6  $\mu m$  from the peening center.

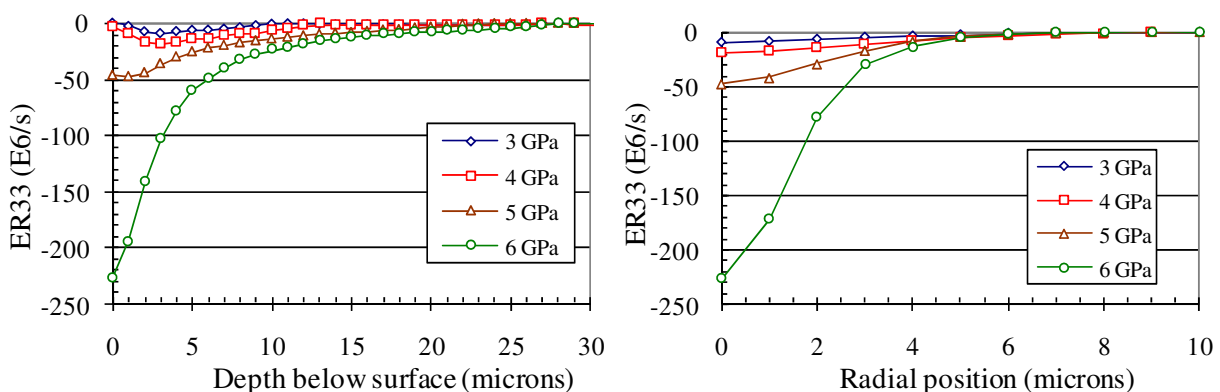


Fig. 15. Strain rate distributions at different peening pressure

#### 4.3 Case 3: LSP simulation of peening biomedical material for enhanced corrosion performance

A 3D semi-infinite model was used to simulate micro scale laser shock peening of biodegradable Mg-Ca. The material constants ( $C_1 - C_{20}$ ) of the biomaterial were determined by fitting the ISV model to the baseline test data using a non-linear square fitting method (Guo et al., 2005). The fitted material constants are shown in Table 3 (Guo & Salahshoor, 2010). The modulus of elasticity for Mg-Ca is 45 GPa. Poisson's ratio is 0.33 at room temperature. The density is  $1750 \text{ kg/m}^3$ .

A series of four simulations were performed in order to simulate sequential LSP. The Mg-Ca surface was peened once per simulation. Each simulation is composed of two steps. In the first step, the shock pressure is applied on the top surface. Next, the stresses and strains are allowed sufficient time to relax so that the solution has time to stabilize. The results from the first simulation were imported to the second simulation and so on until the surface was peened 4 times.

ISV parameter	Material constants	ISV parameter	Material constants
$C_1$ (MPa)	1.0	$C_{11}$ (s/MPa)	1E-4
$C_2$ (K)	600	$C_{12}$ (K)	0
$C_3$ (MPa)	850	$C_{13}$ (1/MPa)	0.7
$C_4$ (K)	20	$C_{14}$ (K)	100
$C_5$ (1/s)	1.0E-7	$C_{15}$ (MPa)	3E4
$C_6$ (K)	0	$C_{16}$ (MPa/K)	39
$C_7$ (1/MPa)	0.1	$C_{17}$ (s/MPa)	380
$C_8$ (K)	-300	$C_{18}$ (K)	-900
$C_9$ (MPa)	2500	$C_{19}$	0.2
$C_{10}$ (MPa/K)	0	$C_{20}$ (K)	312.8

Table 3. ISV material constants of Mg-Ca alloy

#### 4.3.1 Simulation scheme

The 3D model in Figure 16 contains a quarter cylinder of 70,818 C3D8R finite elements and 3,575 CIN3D8 infinite elements. The quarter cylinder mesh allows for a comprehensive analysis of the three dimensional stress and strain behavior below the surface while minimizing the computation time. Infinite elements as quiet boundary along the back and bottom surfaces were implemented to allow for stress waves to pass through a non-reflective boundary.

The mesh has two regions with different mesh densities. As expected, the area where the pressure is applied contains a higher mesh density than the outer regions of the model. The dense mesh region consists of 30  $\mu\text{m}$  wide cubic elements. Micron level elements provide a suitable spatial resolution of the output variables to ensure spatial convergence.

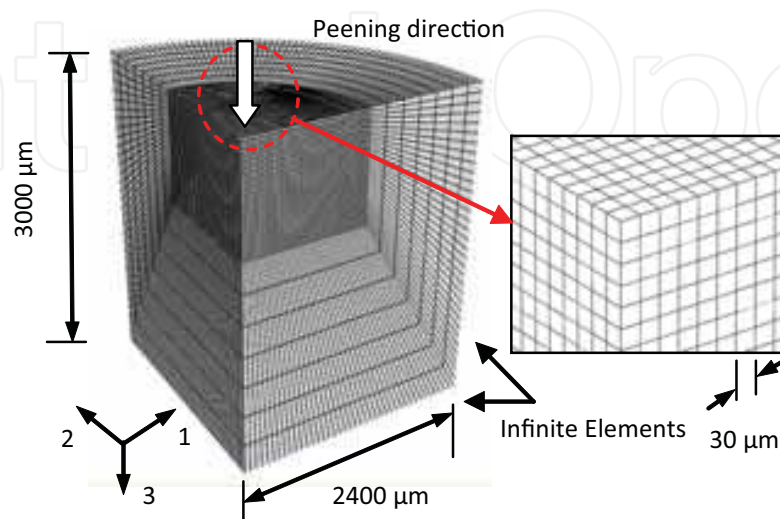


Fig. 16. Three-dimensional FEA simulation of LSP

The pressure induced by LSP is a function of elapsed time and radial position. A useful approximation for  $P(t)$  is to assume it follows a 6<sup>th</sup> order polynomial as shown in Figure 17. The generic profile is based on numerous researchers (Berthe et al., 1997; Fabbro et al., 1990; Devaux et al., 1993; Wu & Shin, 2005; Zhang et al., 2004) who have measured the  $P(t)$  as a function of time. The critical components of  $P(t)$  are the pulse time and the peak pressure. The pressure pulse time typically last 2-3 times longer than the laser pulse (Devaux et al., 1993; Berthe et al., 1999; Zhang & Yao, 2002). For the purpose of these simulations, the pressure pulse was assumed to be 3 times longer than the 7 ns laser pulse. The peak pressure for  $P(t)$  in water confined regime was estimated by

$$P(\text{GPa}) = 0.01 \sqrt{\frac{\alpha}{2\alpha + 3}} \sqrt{Z(\text{g} / \text{cm}^2 \text{s})} \sqrt{I_o(\text{GW} / \text{cm}^2)} \quad (17)$$

where  $P$  is the peak pressure,  $Z$  is combined shock impedance defined by the following Eq. (18),  $I_o$  is the power density given by Eq. (19), and  $a$  is a correction factor for the efficiency of the interaction (Fabbro et al., 1990; Peyre et al., 1996). Since the ablative material used in these experiments was relatively thick and absorbent compared to other materials used in literature,  $a$  was estimated to be low (0.1) such that the majority of the energy was absorbed by the ablative material.  $Z_{\text{MgCa}}$  is defined as the product of the density and shock velocity ( $Z_{\text{MgCa}} = \rho_{\text{MgCa}} U_{\text{MgCa}}$ ). The density of Mg-Ca is 1750 kg/m<sup>3</sup> and the shock velocity is approximated based on the wave speed of sound through Mg-Ca ( $\approx 5000$  m/s).  $Z_{\text{MgCa}}$  and  $Z_{\text{water}}$  are  $8.75 \times 10^5$  and  $1.65 \times 10^5$  g/cm<sup>2</sup>, respectively.

$$\frac{2}{Z} = \frac{1}{Z_{\text{MgCa}}} + \frac{1}{Z_{\text{water}}} \quad (18)$$

$$I_o = \frac{E}{t_p A} \quad (19)$$

where  $E$  is the average energy per pulse given as 0.2667 J.  $t_p$  is the simulated pressure pulse time (21ns).  $A$  is the cross-sectional area of the generated plasma. The diameter of the pressure wave is approximately 250  $\mu\text{m}$  which results in a peak pressure of 5 GPa.

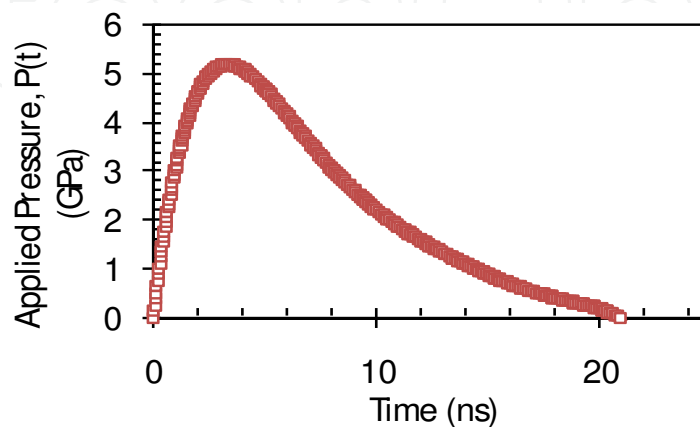


Fig. 17. Spatially uniform shock pressure,  $P(t)$

In this study, the radial expansion of plasma was taken into account for the following reasons. First, the experimental laser spot size is on the order of 100 microns. With such a small spot size, the expansion of plasma may not be neglected in the radial direction. Furthermore, the experimental ablative layer is not fully vaporized because it is thick and absorbs energy well. As a consequence, the pressure wave generated by the plasma has time and space to expand in all directions before entering the metal substrate. Radial expansion of plasma was modeled by allowing the applied pressure to act perpendicular to the deformed surface. Initially the pressure is one dimensional. As deformation occurs, the pressure follows the deformed surface resulting in a spherical shape pressure that expands in the radial direction.

Implementing the temporal and spatial shock pressure is very challenging and a user load subroutine is therefore required. The user subroutine VDLOAD (Warren et al., 2008) of shock pressure has been programmed to apply a non-uniform shock pressure across the top surface. The circular pressure was applied in four locations. Figure 18 shows the peening distribution along the top surface. The spacing between simulated peens is 800  $\mu\text{m}$ .

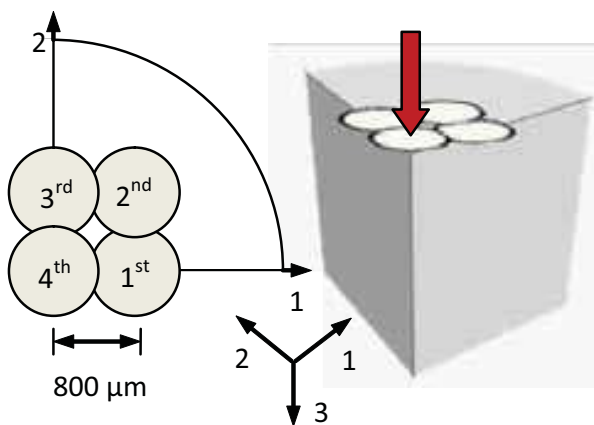


Fig. 18. Sequence of peening simulations (quarter shown)

#### 4.3.2 Simulation results

Material behavior is characterized by stress/strain graphs along the peening or depth direction (axis-3 in Figure 18) and radial directions (axis-1&2). Each stress/strain profile represents the stabilized residual stress/strain. Residual stress/strain was achieved 30  $\mu\text{s}$  after the pressure pulse.

**Dent geometry:** Figure 19a depicts the simulated dent profiles for sequential and single LSP. The diameter of the simulated dents was 600-700  $\mu\text{m}$  and had a depth of 10  $\mu\text{m}$ . There was a negligible effect of neighboring dents on the overall dent depth. However, it was observed that neighboring dents do influence the tensile pile up region. The magnitude of the pile up increased approximately 50%. It is believed to be due to the radial expansion of neighboring peens. Tensile pile up is critical to tribological applications such as implants. A tensile region on the surface can drastically affect the wear and fatigue performance of a surface. Figure 19b shows the experimental dent profiles for sequential and single LSP. The experimental dents also had a diameter between 600-700  $\mu\text{m}$  and a depth of 11  $\mu\text{m}$ . Results from the experiments confirms the validity of the simulation. Figure 19c and 19d are optical images of dents by sequential and single LSP.

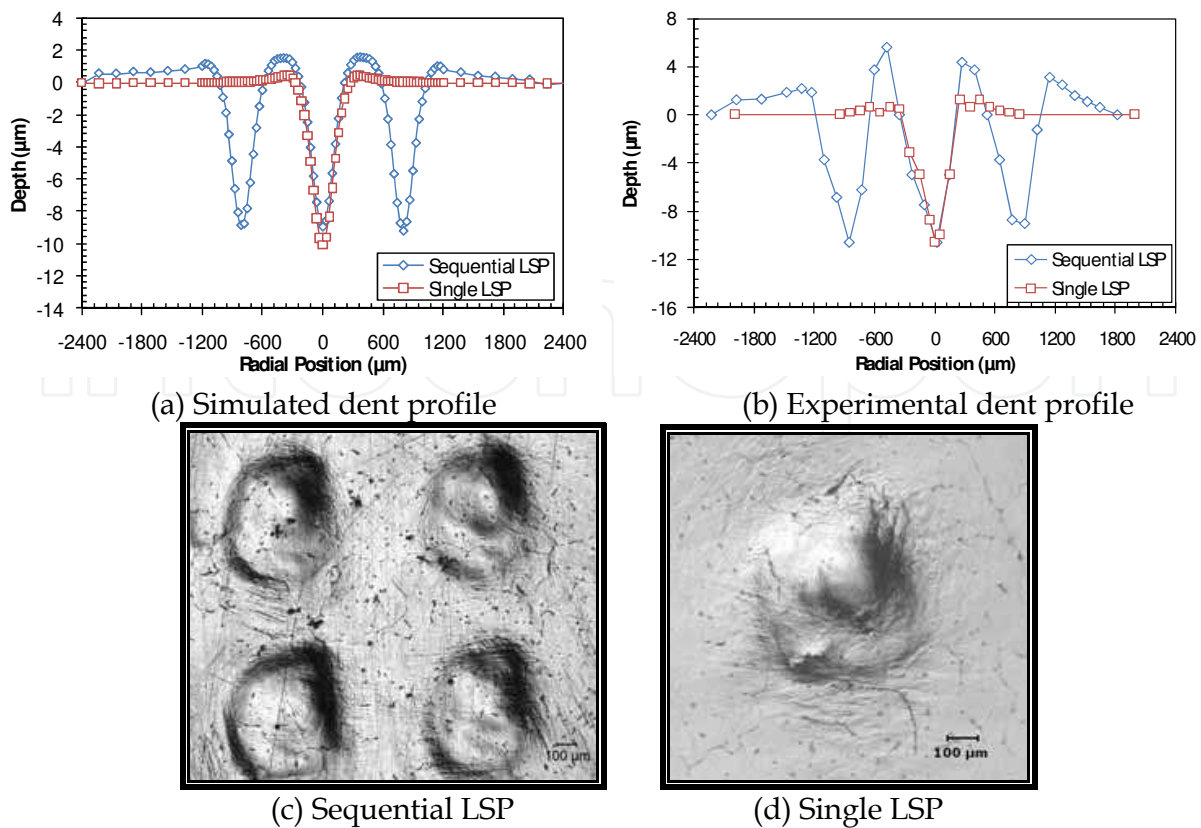


Fig. 19. Simulated and measured dent topography

**Residual stress profiles:** The predicted residual von Mises stress and S33 stress along the depth direction are shown in Figures 20a and 21a. The von Mises stress penetrated deeper into the surface for sequential peening. As expected, sequential peening had a greater effect on the surface residual stress since a larger area was exposed to peening. Along the depth direction, the residual stress S33 is compressive for approximately 150  $\mu\text{m}$ . The compressed region is followed by a tensile region that eventually approaches 0 MPa. The magnitude of the compressive residual stress below the surface is 23 MPa. The predicted residual von Mises stress and S22 stress along the radial direction are shown in Figures 20b and 21b. Single peening neglects the effects from neighboring stress fields on the surface residual stress. Future work will include comparing simulated residual stress profiles to experimental residual stress.

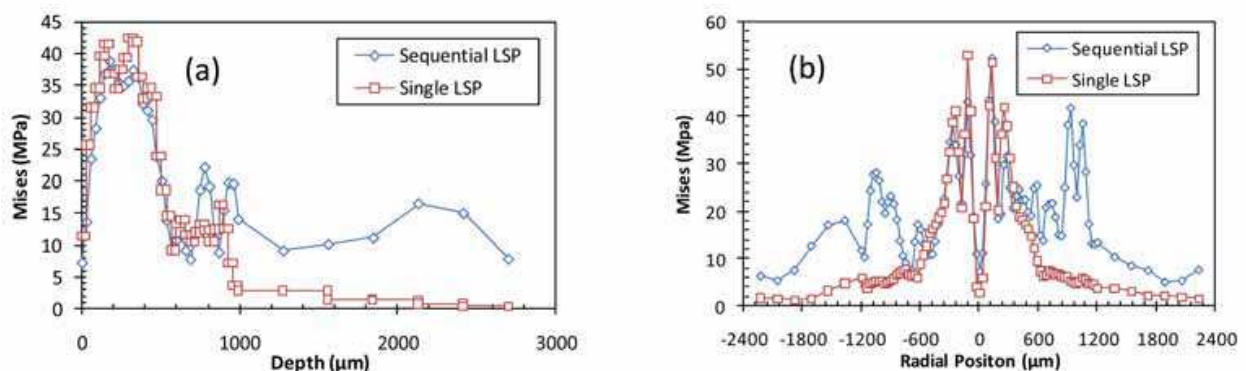


Fig. 20. Residual von Mises stress along depth (a) and radial (b) directions

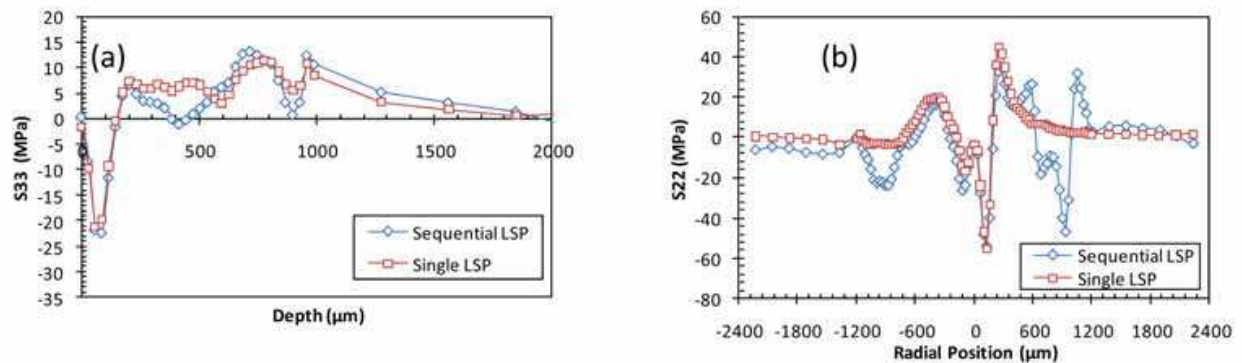


Fig. 21. Residual stress, S33 along depth (a) and S22 along the radial (b) directions

**Strain and strain rate profiles:** The plastic strain in the depth and radial directions is shown in Figure 22. The plastic strain extended 500 μm below the surface. The residual stress from previous peens had a negligible effect on the plastic strain. The maximum plastic strain occurred on the top surface and in the center of the dent. The diameter of the plastic zone is directly related to the topography of the dent. The peak strain rate in peening direction for the simulations was  $19 \times 10^6 \text{ s}^{-1}$  in Figure 23.

This work focuses on the experiment and FEA simulation of LSP MgCa alloy. More experimental results are needed to verify the simulation results. Further work is needed to demonstrate the effectiveness of the resulting surface by this method in improving surgery of bone ailments.

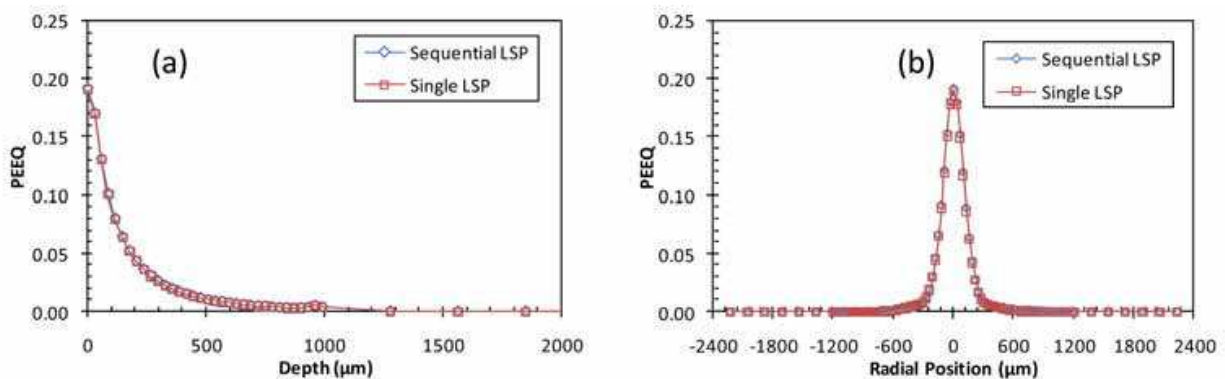


Fig. 22. Equivalent plastic strain PEEQ along depth (a) and radial (b) directions

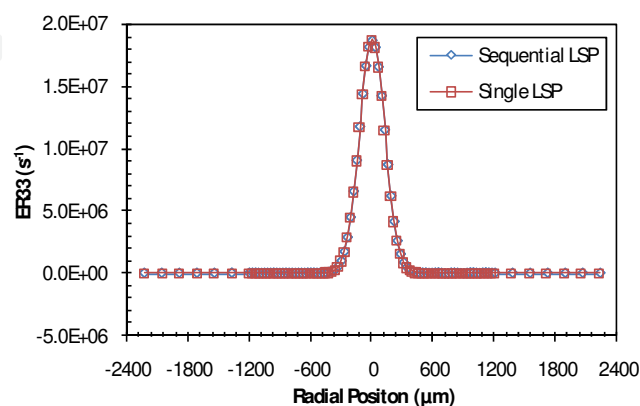


Fig. 23. Strain rate on the top surface, ER33

## 5. Conclusions

Laser shock peening (LSP) is a surface treatment process to improve surface integrity which significantly impacts component performance of fatigue, wear, corrosion, and foreign object damage. This chapter provides a state-of-the-art of LSP simulation and discussed the challenging issues to simulate a LSP process using finite element method. The new contributions of this chapter provide a 3D model of temporal and spatial shock pressure and material user subroutine of dynamic mechanical behavior at high strain rates. Three simulation case studies in automotive, aerospace, and biomedical industries are presented using the developed simulation method. The key results may be summarized as follows.

- The 3D spatial and temporal peening pressure was modeled using a user subroutine.
- The dynamic material behavior at high strain rates was modeled using the ISV model. Material constants of three types of important engineering materials were obtained.
- The simulated dent geometry and residual stresses are similar to the measured data. This suggests the pressure model used successfully characterized the formation and propagation of the pressure wave.
- The results suggested there is an optimal peening time that produces the deepest dent. Pulse time has a significant effect on the strain rate range.
- The maximum transient stress occurred at a certain peening time. The stress along the radial direction was slightly affected by the peening times. However, the stress along the depth and radius were drastically affected by the peak pressures. Increasing the peak pressure resulted in larger and shallower maximum stress.
- Sequential peening affects the dent topography by increasing the size of the tensile pile up region. The pile-up region forms from the radial expansion of plasma. It is believed to have a great significance on tribological aspects of the biodegradable implant material.
- There was no observed effect on the depth of dents when sequential peening was used as opposed to individual peening.

## 6. References

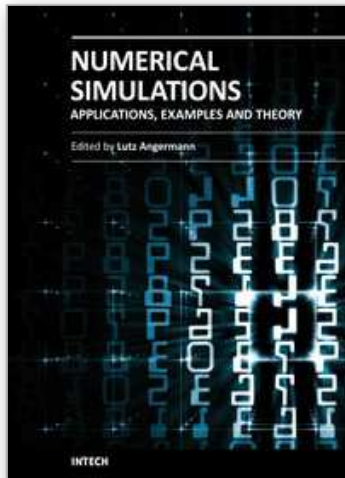
- [1] Fairland, B.P. & Clauer, A.H. (1976). Effect of water and paint coatings on the magnitude of laser-generated shock waves. *Optics Communications*, 14(3), 588-591.
- [2] Fairland, B.P.; Wilcox, B.A.; Gallagher, W.J. & Williams, D.N. (1972). Laser shock-induced microstructural and mechanical property changes in 7075 aluminum. *J. Appl. Phys.*, 43, 3893-3895.
- [3] Fabbro, R.; Fournier, J.; Ballard, P.; Devaux, D. & Virmont, J. (1990). Physical study of laser-produced plasma in confined geometry. *J. App. Physics*, 68, 775-54.
- [4] Masse, J.E. & Barreau, G. (1995). Laser generation of stress waves in metal. *Surf. Coatings Tech.*, 70, 179-191.
- [5] Berthe, L.; Fabbro, R.; Peyre, P.; Tollier, L. & Bartnicki, E. (1997). Shock waves from a water-confined laser-generated plasma. *J. Appl. Phys.*, 82, 2826-2832.
- [6] Fan, Y.; Wang, Y.; Vukelic, S. & Yao, Y.L. (2005). Wave-solid interactions in laser-shocked-induced deformation processes. *J. Appl. Phys.*, 98 (10), 104904-104901-11.
- [7] Warren, A.W.; Guo, Y.B. & Chen, S.C. (2008). Massive parallel micro laser shock peening: simulation, validation, and analysis. *Int. J. Fatigue*, 30, 188-197.

- [8] Caslaru, R.; Sealy, M.P. & Guo, Y.B. (2009). Fabrication and characterization of micro dent array on al 6061-t6 surface by laser shock peening. *Trans. NAMRI/SME*, 37, 159-166.
- [9] Clauer, A.H.; Ford, C.T. & Ford, S.C. (1983). The effects of laser shock processing on the fatigue properties of T-3 aluminum, In: *Lasers in materials processing*, American Society for Metals, 7-22, Metals Park.
- [10] Clauer, A.H. & Koucky, J.R. (1991). Laser shock processing increases the fatigue life of metal parts. *Materials and Processing*, 6, 3-5.
- [11] Peyre, P.; Fabbro, R.; Merrien, P. & Lieurade, H.P. (1996). Laser shock processing of aluminum alloys. Application to high cycle fatigue behavior, *Materials Science and Engineering A*, 210, 102-113.
- [12] Vaccari, J.A. (1992). Laser shocking extends fatigue life. *American Machinist*, 62-64.
- [13] Ashley, S. (1998). Powerful laser means better peening. *Mechanical Engineering*, 120, 12.
- [14] Brown, A.S. (1998). A shocking way to strengthen metal, *Aerospace America*, 21-23.
- [15] Banas, G.; Elsayed-Ali, H.E.; Lawrence, F.V. & Rigsbee, J.M. (1990). Laser shock-induced mechanical and microstructural modification of welded maraging steel. *Journal of Applied Physics*, 67, 2380-2384.
- [16] Fabbro, R.; Peyre, P.; Berthe, L. & Sherpereel, X. (1998). Physics and application of laser-shock processing. *Journal of Laser Applications*, 10, 265-279.
- [17] Peyre, P.; Berthe, L.; Sherpereel, X. & Fabbro, R. (1998). Laser-shock processing of aluminum coated 55C1 steel in water-confinement regime, characterization and application to high-cycle fatigue behavior. *Journal of Materials Science*, 33, 1421-1429.
- [18] Ruschau, J.J.; John, R.; Thompson, S.R. & Nicholas, T. (1999). Fatigue crack nucleation and growth rate behavior of laser shock peened titanium. *International Journal of Fatigue*, 21, 199-209.
- [19] Zhang, W.; Yao, Y.L. & Noyan, I.C. (2004). Microscale laser shock peening of thin films, Part 1: Experiment modeling and simulation. *Journal of Manufacturing Science and Engineering*, 126, 10-17.
- [20] Clauer, A.H. & Holbrock, J.H. (1981). Effects of laser induced shock waves on metals, *Proceedings of Shock Waves and High Strain Phenomena in Metals-Concepts and Applications*, pp. 675-702, Plenum, New York.
- [21] Braisted, W. & Brockman, R. (1999). Finite element simulation of laser shock peening. *International Journal of Fatigue*, 21, 719-724.
- [22] Ding, K. & Ye, L. (2003). Three-dimensional dynamic finite element analysis of multiple laser shock peening process. *Surface Engineering*, 19, 351-358.
- [23] Zhang, W. & Yao, Y.L. (2002). Micro scale laser shock processing of metallic components. *Journal of Manufacturing Science and Engineering*, 124, 369-378.
- [24] Anderson, P.; Koskinen, J.; Varjus, S.; Gerbig, Y.; Haefke, H.; Georgiou, S.; Zmhad, B. & Buss, W. (2007). Microlubrication effect by laser-textured steel surfaces, *Wear*, 262, 369-379.
- [25] Romano, V.; Weber, H.P.; Dumitru, G.; Pimenov, S.; Kononenko, T.V.; Konov, V.; Haefke, H. & Gerbig, G. (2003). Laser surface microstructuring to improve tribological systems. *Proceedings of the SPIE*, 5121, 199-211.
- [26] Nakatsuji, T. & Mori, A. (2001). The Tribological Effect of Electrolytically Produced Micro-pools and Phosphoric Compounds on Medium Carbon Steel Surfaces in Rolling-Sliding Contact. *Tribology Transactions*, 44, 173-178.

- [27] Friedrich, C.R. (2002). Micromechanical machining of high aspect ratio prototypes. *Microsystem technologies*, 8, 343-347.
- [28] Etsion, I. (2005). State of Art in Laser Surface Texturing. *Journal of Tribology*, 127, 248-253.
- [29] Benli, S.; Aksoy, S.; Havitcioglu, H. & Kucuk, M. (2008). Evaluation of bone plate with low stiffness material in terms of stress distribution. *Journal of Biomechanics*, 41, 3229-3235.
- [30] Completo, A.; Fonseca, F. & Simoes, J.A. (2008). Strain shielding in proximal tibia of stemmed knee prosthesis: experimental study. *Journal of Biomechanics*, 41, 560-566.
- [31] Au, A.G.; Raso, V.J.; Liggins, A.B. & Amirfazli, A. (2007). Contribution of loading conditions and material properties to stress shielding near the tibial component of total knee replacements. *Journal of Biomechanics*, 40, 1410-1416.
- [32] Shi, J.F.; Wang, C.J.; Laoui, T.; Hart, W. & Hall, R. (2007). A dynamic model of simulating stress distribution in the distal femur after total knee replacement, *Proceedings of the Inst MECH E Part H, Journal of Engineering in Medicine*, 221, 903-912.
- [33] Isaksson, H. & Lerner, A.L. (2003). Mathematical modeling of stress shielding with bioresorbable materials for internal fracture fixation, *Proceedings of Bioengineering Conference*, 1041-1042, Key Biscayne, Florida.
- [34] Nagels, J.; Stokdijk, M. & Rozing, P. M. (2003). Stress shielding and bone resorption in shoulder arthroplasty. *Journal of Shoulder and Elbow Surgery*, 12, 35-39.
- [35] Gefen, A. (2002). Computational simulations of stress shielding and bone resorption around existing and computer-designed orthopedic screws. *Medical & Biological Engineering & Computing*, 40, 311- 322.
- [36] Seiler, H. G. (1987). *Handbook on Toxicity of Inorganic Compounds*, CRC Press.
- [37] Song, G. (2007). Control of biodegradation of biocompatible magnesium alloys. *Corrosion Science*, 49, 1696-1701.
- [38] Ilich, J. Z. & Kerstetter, J. E. (2000). Nutrition in bone health revisited: a story beyond calcium. *Journal of the American College of Nutrition*, 19, 715-737.
- [39] Aksakal., B. & Hanyaloglu, C. (2008). Bioceramic dip-coating on Ti-6Al-4V and 316L SS implant materials. *Journal of Materials Science: Materials in Medicine*, 19, 2097-2104.
- [40] Warren, A.W.; Guo, Y.B. & Chen, S.C. (2005). A numerical simulation of massive parallel laser shock peening, *Proc. of ASME International Mechanical Engineering Congress & Exposition*, Orlando, FL.
- [41] Warren, A.W. & Guo, Y.B. (2007). FEA modeling and analysis of 3d pressure and mechanical behavior at high strain rate in micro laser peening. *Trans. NAMRI/SME*, 35, 409-416.
- [42] Sealy, M.P. & Guo, Y.B. (2008). Fabrication and finite element simulation of  $\mu$ -laser shock peening for micro dents. *Int. J. Comp. Methods in Eng. Sci. & Mech.*, 10, 149-157.
- [43] Bammann, D.J.; Chiesa, M.L.; Horstemeyer, M.F. & Weingarten, L.I. (1993). Failure in ductile materials using finite element methods, In: *Structural Crashworthiness and Failure*, Jones, N. & Weirzbicki, T. (Eds.), 1-54, Elsevier, 1851669698, Amsterdam.
- [44] Bammann, D.J.; Chiesa, M.L. & Johnson, G.C. (1996). Modeling large deformation and failure in manufacturing processes, In: *19th International Congress on Theoretical and Applied Mechanics*, Tatsumi, T., Watanabe, E. & Kambe, T., (Eds.), 359-376, Elsevier, Amsterdam.

- [45] HKS, Inc. (2008). *ABAQUS User's Manual, Ver. 6.4*, Pawtucket, RI .
- [46] Guo, Y.B.; Wen, Q. & Horstemeyer, M.F. (2005). An Internal State Variable Plasticity Based Approach to Determine Dynamic Loading History Effects in Manufacturing Processes. *Int. J. Mech. Sci.*, 47, 1423-1441.
- [47] Guo, Y.B. & Salahshoor, M. (2010). Process Mechanics and Surface Integrity by High-Speed Dry Milling of Biodegradable Magnesium-Calcium Implant Alloys. *Ann. CIRP*, 59/1, 151-154.
- [48] Devaux, D.; Fabbro, R.; Tollier, L. & Bartnicki, E. (1993). Generation of shock waves by laser-induced plasma in confined geometry. *Journal of Applied Physics*, 74, 2268-2273.
- [49] Wu, B. & Shin, Y. (2005). A self-closed thermal model for laser shock peening under the water confinement regime configuration and comparisons to experiments. *Journal of Applied Physics*, 97, 1-12.
- [50] Berthe, L.; Fabbro, R.; Peyre, P. & Bartnicki, E. (1999). Wavelength dependent laser shock-wave generation in the water-confinement regime. *Journal of Applied Physics*, 85-11, 7552-7555.

IntechOpen



## **Numerical Simulations - Applications, Examples and Theory**

Edited by Prof. Lutz Angermann

ISBN 978-953-307-440-5

Hard cover, 520 pages

**Publisher** InTech

**Published online** 30, January, 2011

**Published in print edition** January, 2011

This book will interest researchers, scientists, engineers and graduate students in many disciplines, who make use of mathematical modeling and computer simulation. Although it represents only a small sample of the research activity on numerical simulations, the book will certainly serve as a valuable tool for researchers interested in getting involved in this multidisciplinary field. It will be useful to encourage further experimental and theoretical researches in the above mentioned areas of numerical simulation.

### **How to reference**

In order to correctly reference this scholarly work, feel free to copy and paste the following:

Y.b. Guo (2011). Laser Shock Peening: Modeling, Simulations, and Applications, Numerical Simulations - Applications, Examples and Theory, Prof. Lutz Angermann (Ed.), ISBN: 978-953-307-440-5, InTech, Available from: <http://www.intechopen.com/books/numerical-simulations-applications-examples-and-theory/laser-shock-peening-modeling-simulations-and-applications>

**INTECH**  
open science | open minds

### **InTech Europe**

University Campus STeP Ri  
Slavka Krautzeka 83/A  
51000 Rijeka, Croatia  
Phone: +385 (51) 770 447  
Fax: +385 (51) 686 166  
[www.intechopen.com](http://www.intechopen.com)

### **InTech China**

Unit 405, Office Block, Hotel Equatorial Shanghai  
No.65, Yan An Road (West), Shanghai, 200040, China  
中国上海市延安西路65号上海国际贵都大饭店办公楼405单元  
Phone: +86-21-62489820  
Fax: +86-21-62489821

© 2011 The Author(s). Licensee IntechOpen. This chapter is distributed under the terms of the [Creative Commons Attribution-NonCommercial-ShareAlike-3.0 License](https://creativecommons.org/licenses/by-nc-sa/3.0/), which permits use, distribution and reproduction for non-commercial purposes, provided the original is properly cited and derivative works building on this content are distributed under the same license.

IntechOpen

IntechOpen